Journal of Nuclear Materials 402 (2010) 186–195

Contents lists available at ScienceDirect

Journal of Nuclear Materials

journal homepage: www.elsevier.com/locate/jnucmat

Carburization behavior of AISI 316LN austenitic stainless steel – Experimental studies and modeling

C. Sudha [a], N. Sivai Bharasi [b], R. Anand [a], H. Shaikh [b,*], R.K. Dayal [b], M. Vijayalakshmi [a]

[a] Physical Metallurgy Division, Metallurgy and Materials Group, Indira Gandhi Centre for Atomic Research, Kalpakkam 603 102, Tamilnadu, India
[b] Corrosion Science and Technology Division, Metallurgy and Materials Group, Indira Gandhi Centre for Atomic Research, Kalpakkam 603 102, Tamilnadu, India

ARTICLE INFO

Article history:
Received 9 October 2009
Accepted 24 May 2010

ABSTRACT

AISI type 316LN austenitic stainless steel was exposed to flowing sodium at 798 K for 16,000 h in the bimetallic (BIM) sodium loop. A modified surface layer of 10 μm width having a ferrite structure was detected from X-ray diffraction and electron micro probe based analysis. Beneath the modified surface layer a carburized zone of 60 μm width was identified which was found to consist of $M_{23}C_6$ carbides. A mathematical model based on finite difference technique was developed to predict the carburization profiles in sodium exposed austenitic stainless steel. In the computation, effect of only chromium on carbon diffusion was considered. Amount of carbon remaining in solution was determined from the solubility parameter. The predicted profile showed a reasonably good match with the experimental profile. Calculations were extended to simulate the thickness of the carburized layer after exposure to sodium for a period of 40 years. Attempt was also made to predict the carburization profiles based on equilibrium calculations using Dictra and Thermocalc which contain both thermodynamic and kinetic databases for the system under consideration.

1. Introduction

In fast breeder reactors liquid sodium is used as a coolant in the primary as well as the secondary circuit due to its favorable properties like high thermal conductivity, low vapour pressure, high boiling point, high heat capacity and low absorption cross section for fast neutrons. Austenitic stainless steels of different grades are used as structural materials in the primary circuit, intermediate heat exchanger (IHX) and piping in secondary loop because of their compatibility with liquid sodium and adequate high temperature mechanical properties. In the prototype fast breeder reactor (PFBR), AISI type 316LN stainless steel has been selected as structural material in the primary circuit in order to circumvent the problem of sensitization and related aqueous corrosion issues during fabrication and storage. For such critical application it is essential to know the extent of corrosion and mass transfer suffered by 316LN austenitic stainless steel in flowing sodium.

Though localized electrochemical corrosion of structural materials is absent in sodium, long term exposure can degrade their mechanical properties due to mass transfer and corrosion which manifest through the following processes [1]:

1. Complete loss of material due to leaching leading to reduction in wall thickness.
2. Preferential leaching of elements forming modified surface layer.
3. Formation of a carburized or decarburized layer beneath the modified surface layer depending on the carbon activity difference between sodium and steel, temperature, and duration of exposure.

Presence of non-metallic impurities like oxygen and carbon in sodium significantly influences the corrosion of austenitic stainless steel. When oxygen concentration is less than 10 wppm, chromium present in steel can combine with oxygen and sodium to form a ternary compound namely $NaCrO_2$ [2]. For higher oxygen concentrations formation of ternary compounds of other transition metals has been observed [3]. Several reports are available on the preferential leaching of elements from structural materials in flowing sodium leading to changes in heat transport and mechanical properties [4–6].

If carbon is present, sodium can either carburize or decarburize the structural material depending on whether its carbon activity is lower or higher than that in steel. Several countries in the world have carried out experiments in flowing sodium with very low carbon concentrations in order to assess the extent of corrosion and mass transfer and the consequent changes in mechanical properties [4,7,8]. In addition to the experimental studies attempts have been made to model the carburization/decarburization process also. Farkas and Delgado [9] modeled the carburization process in stainless steel by taking into consideration the cross diffusion

* Corresponding author. Tel.: +91 44 27480121; fax: +91 44 27480202.
E-mail address: hasan@igcar.gov.in (H. Shaikh).

0022-3115/$ - see front matter © 2010 Elsevier B.V. All rights reserved.
doi:10.1016/j.jnucmat.2010.05.023

coefficient terms which account for the influence of substitutional alloying elements on carbon diffusion. Bongartz et al. [10] predicted the carburization profiles in Fe–32Ni–20Cr–Ti–Al high temperature alloy. In this study even though the cross diffusion terms were not considered precipitation of two different carbide phases was accounted for using the solubility product. The model was used to predict the carburization profiles in a 15 mm thick tube made of alloy 800 H exposed to carburizing atmosphere at 1173 K up to 1,00,000 h. Bongartz et al. [11] further extended the model using finite difference method (FDM) to describe carburization in binary, ternary and quaternary systems of high temperature alloys. In this model coexistence of three different carbide phases was considered. To minimize the assumptions made during computation using FDM a general model was proposed using DICTRA and THERMOCALC which takes into consideration both thermodynamic and kinetic databases for the simulation [12]. The model was successfully used to treat carburization in Ni–Cr and Ni–Cr–Fe systems as well as to predict carbon diffusion profiles in 1CrMoV/12CrMoV dissimilar weldments using the approach of multicomponent diffusion in multiphase dispersions.

The observations and predictions made in the literature cannot be extended to the present study since the Indian sodium contains relatively high concentration of carbon of the order of 25 wppm. The authors have investigated in detail [13,14] the behavior of primary circuit materials in liquid sodium containing 25 wppm of carbon by employing a monometallic sodium loop called as the Mass Transfer Loop (MTL). To get further insight into the long term carburization/decarburization behavior of steels in the simulated environment of the secondary circuit of PFBR (comprising the IHX and steam generator) a bi-metallic (BIM) sodium loop was constructed.

This paper deals with a study on the carburization behavior of AISI type 316LN austenitic stainless steel exposed to liquid sodium in the BIM loop at a temperature of 798 K for 16,000 h. Both experiments and theoretical calculations have been carried out to determine the extent of carburization possible in stainless steel.

2. Experimental procedures

Schematic layout of the BIM loop designed to simulate the secondary circuit of PFBR is shown in Fig. 1. The loop was constructed using AISI type 316LN austenitic stainless steel and Mod.9Cr–1Mo ferritic steel. Sodium was circulated through the loop with the help of an electromagnetic pump capable of generating the desired flow rate of 1.78 m^3/h. Velocity of sodium in the test section was maintained at 2.5 m/s. Cross sectional view of the sample holder which is made of 316LN austenitic stainless steel used to expose 316LN stainless steel test specimens to sodium is given as Fig. 2. To differentiate between thermal ageing and sodium effects separate set of specimens were kept in the sample holder which were not exposed to sodium. Composition of 316LN austenitic stainless steel used in the present study is given in Table 1. Temperature of exposure to sodium was chosen as 798 K which corresponds to the outlet temperature of IHX and inlet temperature of steam generator.

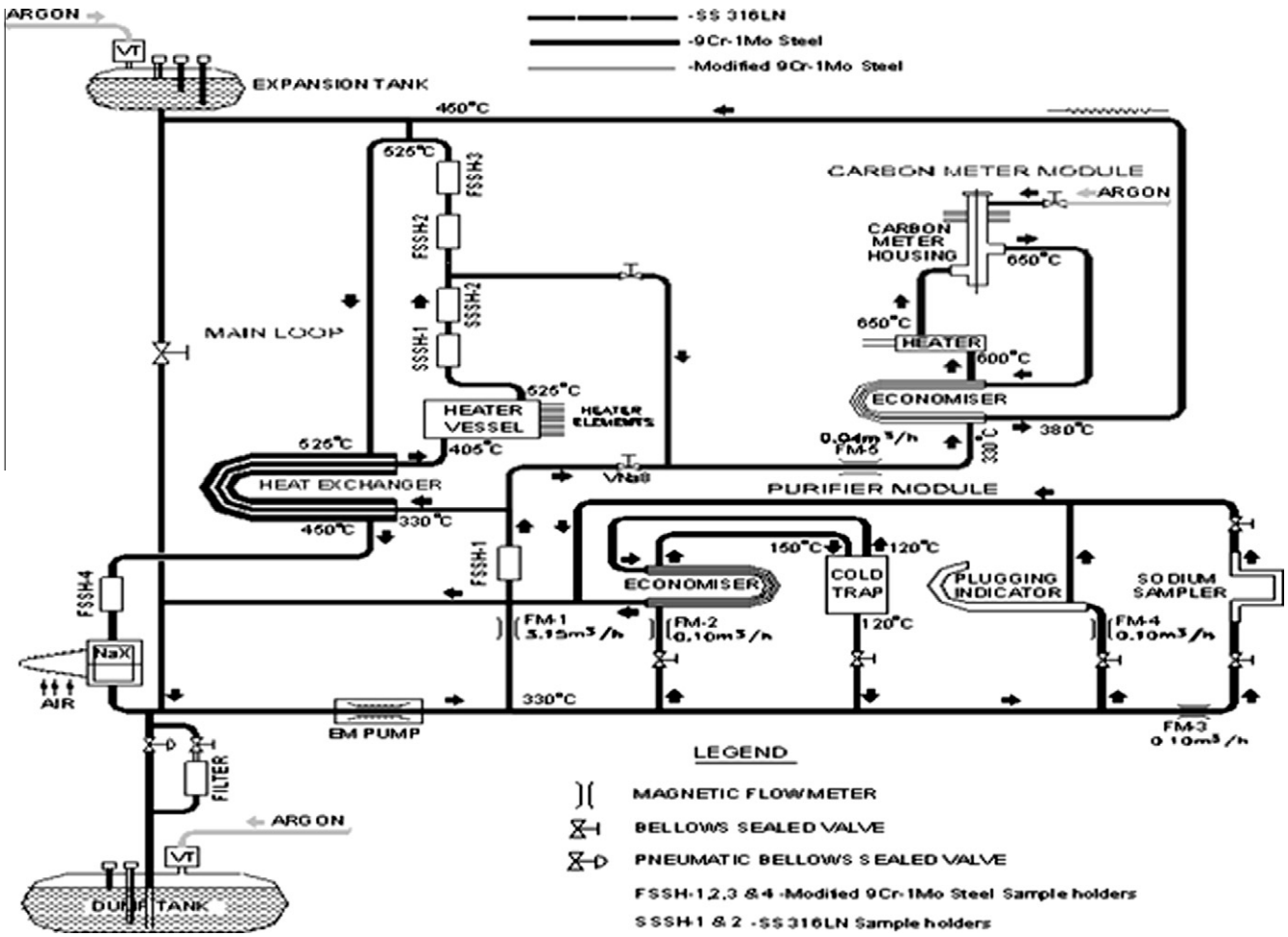

Fig. 1. Schematic layout of BIM loop.

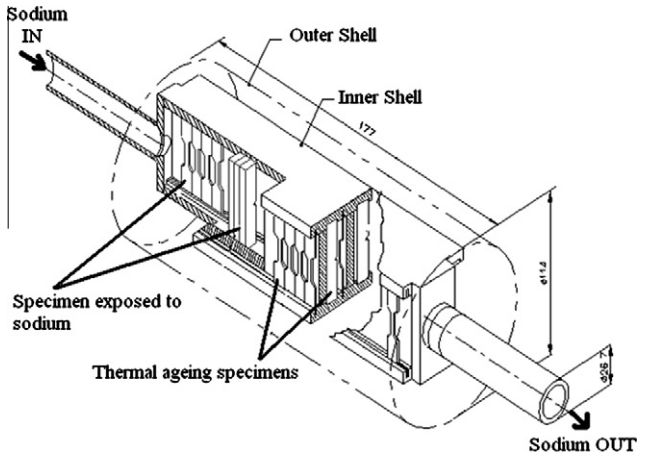

Fig. 2. Cross sectional view of the sample holder used to expose test specimens to sodium in the BIM loop.

Table 1
Chemical composition of 316LN stainless steel used in the present study.

Element in wt%								
C	Ni	Cr	Mo	Si	Mn	N	S	P
0.03	11.2	16	2.0	0.6	1.3	0.085	0.005	0.042

After 16,000 h of exposure, the sample holder was removed from the loop to examine the specimens for sodium effects. The samples were cleaned with alcohol before microstructural and microchemical characterization. Cross section of the samples was prepared by conventional metallographic procedure and electrolytically etched using 10% ammonium persulphate solution at a current of 1 A/cm^2 for 1.5 min. Microstructural examination was carried out using scanning electron microscope (SEM) (Model No.: XL 30 ESEM of M/s FEI, The Netherlands). Stoe powder diffractometer in the GIXRD mode was used for identifying the phases present on the surface (maximum up to 1 μm) of sodium exposed samples. Cu Kα was used as the incident radiation at 40 kV and 30 mA. Angular 2θ range from 10° to 90° was covered with a step size of 0.012°. Various phases present on the surface were identified by comparing the XRD spectrum with standard JCPDF patterns available for corresponding phases.

To identify the corrosion products which might have formed on the surface of sodium exposed specimens X-ray photo electron spectroscopy (XPS of M/s SPECS make, Germany) was used. XPS is a surface analysis technique where only few angstroms of the surface layers are analysed unlike X-ray diffraction where the analyzed volume is much deeper (in μm range). XPS analysis was carried out in an ultra high vacuum chamber maintained at a pressure of 2.9×10^{-9} mbar. Al Kα with a binding energy of 1486.74 eV was used as the primary source of X-rays to generate photo electrons from the sample. The monochromatic source had a resolution of 0.59 eV at an intensity of 285.7 kcps. Photoelectrons emitted from the samples were analyzed using a PHOIBOS 150 MCD hemispherical analyzer with a pass energy of 12 eV for high resolution scans. Contamination if any present on the surface of the specimen was removed by sputtering with argon ions having energy of 5 kV. Photo electron spectra for chromium, iron, nickel, carbon and oxygen were recorded. To identify individual components in each spectrum the high resolution spectra were de-convoluted using CASA XPS software. The chemical state of each element was identified by comparing the binding energy obtained after de-convolution with the standard values available in XPS hand book.

Elemental redistribution across the cross section of sodium exposed specimens was determined using Cameca SX50 electron probe micro analyzer (EPMA). Accelerating voltage of 20 kV and beam current of 20 nA was used for the analysis of iron, chromium and nickel whereas 10 kV and 20 nA was used for the analysis of carbon. Crystals used were LiF for Fe Kα, Cr Kα and Ni Kα and PC2 for C Kα. X-ray generation volume was restricted to ~1 μm. Quantitative analysis was performed by comparing the intensities of Kα radiation of the elements obtained from the sample with that of the standards. A specialized computer package called as 'QUANTA' was used for quantitative analysis which takes care of the corrections to be incorporated while calculating the concentrations of various elements. The carbon concentration profiles were corrected using a calibration graph [15] to avoid overestimation due to contamination.

3. Results and discussion

3.1. Analysis of the carburized layer – experimental studies

SEM microstructure of mill annealed 316LN austenitic stainless steel which was not exposed to sodium revealed a normal austenite structure with an average grain size of 60 μm as shown in Fig. 3. After exposure to sodium a modified layer (marked as 'M' in Fig. 4) having <10 μm width developed on the surface. Beneath the modified surface layer up to a distance of ~60 μm the material had a deformed microstructure (marked as 'D' in Fig. 4) beyond which the structure corresponded to that of the base material. Presence of a modified surface layer has been observed earlier in sodium exposed 316 stainless steel [16]. X-ray diffraction pattern obtained from the surface of sodium exposed steel (Fig. 5) showed the presence of predominantly α (ferrite) phase in addition to γ (austenite), $Cr_{23}C_6$ and Cr_2O_3. Predominant peak for α phase confirmed the modified surface layer to be ferrite. The underlying layer with a deformed structure (marked as 'D' in Fig. 4) was found to be austenite with $Cr_{23}C_6$ precipitates. Chromium rich precipitates will be distributed along grain boundaries and preferred crystallographic planes in austenitic stainless steel. During etching with 10% ammonium per sulphate solution the carbides dissolve giving rise to a ditch structure with thicker outlines along grain boundaries and twins as shown in Fig. 4. Precipitation of high number density of carbides introduces considerable strain in the lattice resulting in the deformation of the material. The Cr_2O_3 signal would have come from the oxide layer which forms on the specimen surface after removal from the BIM loop and exposure to air.

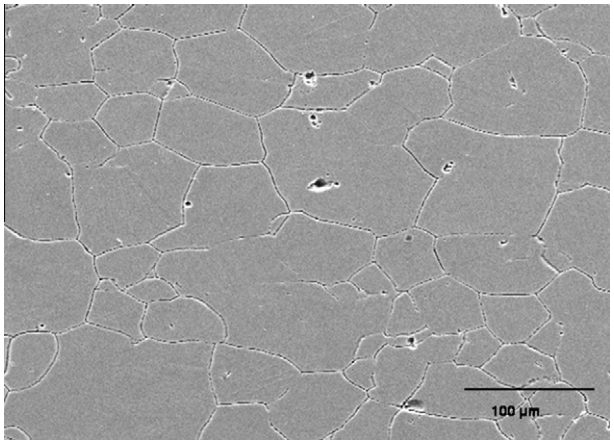

Fig. 3. Microstructure of 316LN austenitic stainless steel before exposure to sodium.

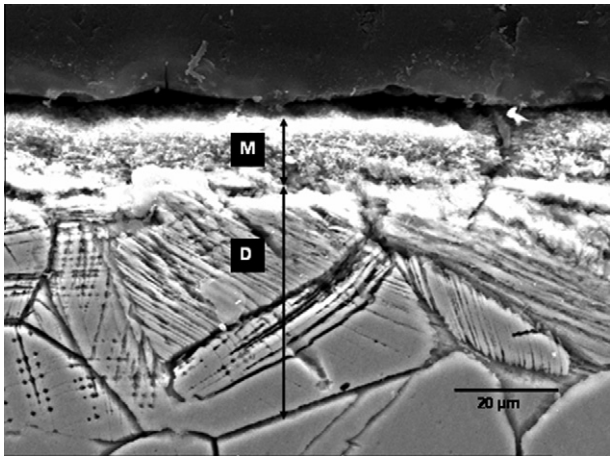

Fig. 4. Cross sectional view of 316LN austenitic stainless steel showing a modified surface layer (marked as 'M') and deformed structure beneath 'M' (marked as 'D') after exposure to sodium.

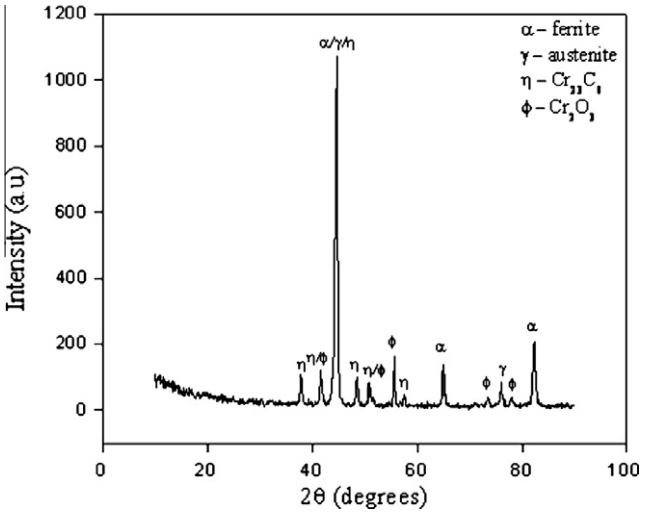

Fig. 5. XRD pattern showing the presence of predominantly the ferrite phase in addition to austenite, $Cr_{23}C_6$ and Cr_2O_3 phases on the surface of sodium exposed stainless steel.

Figs. 6a–6e show the high resolution XPS spectra for carbon, oxygen, chromium, iron and nickel obtained from the surface of sodium exposed steel respectively. De-convoluted high resolution spectrum for carbon (Fig. 6a) showed the presence of adventitious hydrocarbon (C 1s) at a binding energy (BE) of 285 eV. In addition, hydroxides at 286.6 eV and chromium carbides at 283 eV were also found to be present. BE positions are in accordance with the data reported in literature [17]. Curve fitted O 1s spectrum (Fig. 6b) suggests that the surface of the substrate is mainly covered with hydroxide at a BE of 532.9 eV, Fe oxide at 530.2 eV, Cr oxide at 532 eV as well as O 1s peak at 531.2 eV. The relative contribution of each oxygen peak to the total oxygen signal is 48%, 15%, 17% and 20% in the same order as stated earlier. These results compare well with reported values for the O 1s BEs in hydroxide, Fe oxide, Cr oxide and O 1s at 532.8, 530.2, 531.5 and 531 eV respectively [17]. Formation of hydroxides and oxides on the specimen surface may be a result of washing and subsequent exposure to air after removal from the BIM loop. Presence of Cr oxide (at a BE of 576 eV) was also revealed in the peak fitted high resolution spectrum for Cr (Fig. 6c) in addition to the peak corresponding to elemental Cr at 574.4 eV. Contribution of the oxide and elemental peak to the ma-

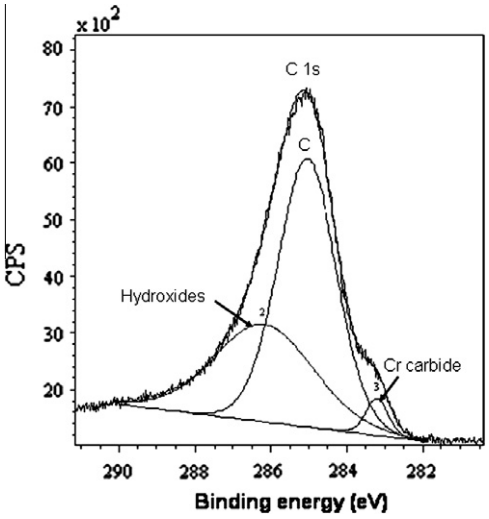

Fig. 6a. De-convoluted high resolution XPS spectra for C 1s.

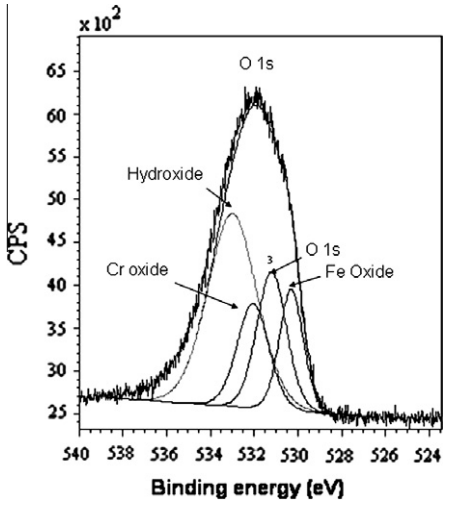

Fig. 6b. De-convoluted high resolution XPS spectra for O 1s.

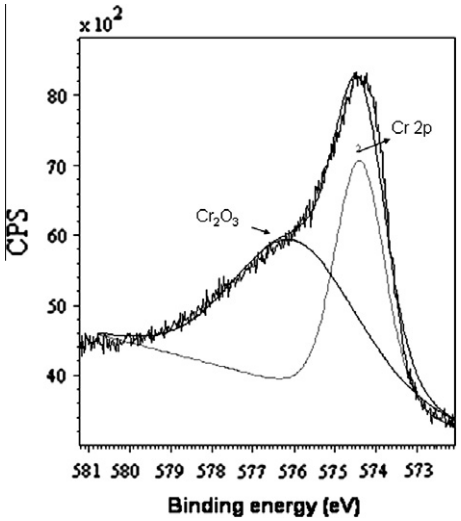

Fig. 6c. De-convoluted high resolution XPS spectra for Cr 2p.

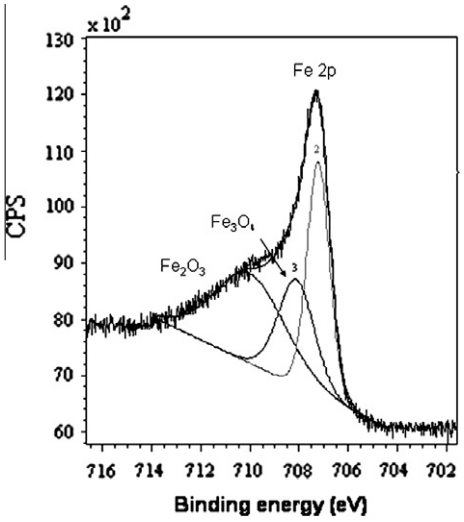

Fig. 6d. De-convoluted high resolution XPS spectra for Fe 2p.

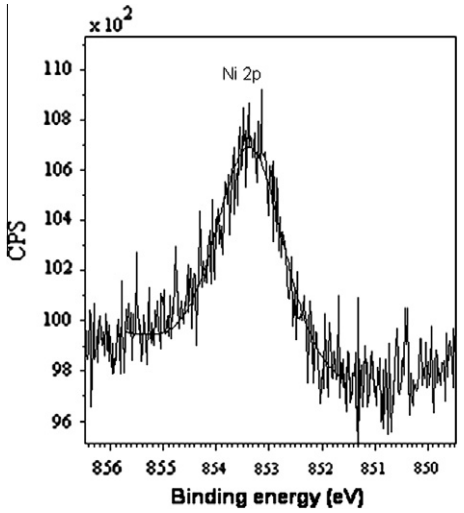

Fig. 6e. De-convoluted high resolution XPS spectra for Ni 2p.

jor Cr 2p peak was 60% and 40% respectively. Even though the analysis of C 1s peak (Fig. 6a) suggested the presence of Cr carbides, no such evidence could be obtained from the Cr 2p peak. It is suggested in literature [18] that Cr $2p_{3/2}$ peak corresponding to Cr–C binding energy should appear near 574.5 eV which lies closer to the recorded elemental Cr 2p peak at 574.4 eV. Since the difference in binding energy (~0.1 eV) is less than the resolution limit of the analyzer well resolved Cr carbide peak could not be obtained. Peak fitted Fe 2p peak (Fig. 6d) showed the presence of Fe_3O_4 at a BE of 708.12 eV, Fe_2O_3 at 710 eV and Fe 2p at 707.2 eV. Binding energy values reported in literature [17] for Fe_3O_4, Fe_2O_3 and Fe are 708.2, 710.9 and 707 eV respectively. Analysis of the high resolution spectrum for nickel revealed its presence only in the elemental form at a BE of 853 eV which is close to the value reported [17] for Ni 2p peak at 852.7 eV. XPS analysis confirmed the absence of ternary oxides of Na and Cr which are expected to form for lower oxygen concentrations [2]. The oxygen content in sodium was probably below the threshold level required for the formation of ternary compounds or they would have got removed during the cleaning process. It is also possible that the formation of hydroxides and oxides on the surface of the specimen might have interfered with the surface analysis.

While X-ray diffraction based investigation revealed the presence of only Cr_2O_3 (Fig. 5) XPS analysis (Fig. 6) showed various types of oxides. Olsson and Landolt [19] have proposed a layered model for the passive films formed on austenitic stainless steel. The peaks corresponding to hydroxides and Fe oxides detected in the XPS analysis (Fig. 6) are from the outermost layer of the passive film which may be only few angstroms thick. Cr oxides are found to be the predominant species in the passive layers of austenitic stainless steels making up the thick second layer of the passive film. Since the contribution from Fe oxides and hydroxides is very small it is possible that XRD would not have been able to detect it. It was found during the course of XPS experiments that even a 1 min sputtering using Ar ions was sufficient to remove the hydroxide and Fe oxide peaks from the spectrum which confirms that they are present only on the topmost layer of the passive film having a thickness of ~10 A°.

To determine the effect of leaching by sodium on the surface, elemental redistribution for Cr, Fe and Ni was determined using an electron microprobe (Fig. 7). From Fig. 7 it is evident that Ni concentration in the ferrite layer is less (~9.2 wt%) compared to that of the base material (~11 wt%). Concentration of chromium and iron in the ferrite layer was ~17.5 and 68 wt% respectively. Depletion of Ni in the modified layer (marked as 'M' in Fig. 4) and subsequent formation of ferrite as confirmed by XRD pattern (Fig. 5) can be understood as follows: in a dynamic sodium loop constituent elements of steel will get continuously leached by sodium from the high temperature components and get transported and deposited in the cooler regions of the loop [20]. Preferential leaching has been observed in the case of Ni since it has higher solubility in sodium (~2 wppm at 798 K) [1]. Due to the depletion of Ni the austenite structure will become unstable resulting in the formation of a ferrite layer on the surface. Preferential leaching to this extent has not been observed in the case of other alloying elements like iron and chromium. This is because of their relatively less solubility in sodium (for e.g.: 0.01 wppm for Cr at 798 K) and also higher probability for the formation of ternary oxides depending upon the oxygen concentration [21].

Fig. 8 shows the carbon concentration profile obtained using the electron microprobe. To avoid overestimation of carbon due to contamination a calibration graph was constructed between true and observed carbon contents using standards, details of which are given elsewhere [15]. All data points in the 'as recorded' profile were re-evaluated using the calibration graph to obtain true carbon concentration values as given in Fig. 8. Carbon concentration decreased from ~0.5 to ~0.4 wt% on the ferrite layer because of the lower solubility of carbon in ferrite. In the carburized layer carbon concentration remained constant at ~0.5 wt% up to a distance of 20 μm beyond which it continuously decreased to reach the matrix composition at a depth of ~60 μm from the surface. Electron microprobe analysis has confirmed the surface carburization of austenitic stainless steel when exposed to sodium in the high temperature section of the BIM loop.

When austenitic stainless steel is exposed to sodium it can get carburized or decarburized depending on the carbon activity difference between sodium and steel. If the activity of carbon in sodium is more, then the steel will get carburized otherwise it will get decarburized. Temperature dependence of carbon solubility in liquid sodium (C_{Na}^{sat}) is expressed using Longson and Thorley's expression [22] as follows:

$$C_{Na}^{sat}(\text{wppm}) = 5.03 \times 10^7 \ \exp\left(-13740/T\right) \quad (1)$$

From Eq. (1) the value for C_{Na}^{sat} at a temperature of 798 K was obtained as 2 wppm. It has been reported [23] that in sodium containing 0.15 wppm of carbon at a temperature of 773 K the carbon activity (a_C) is of the order of 0.1. This value is much higher

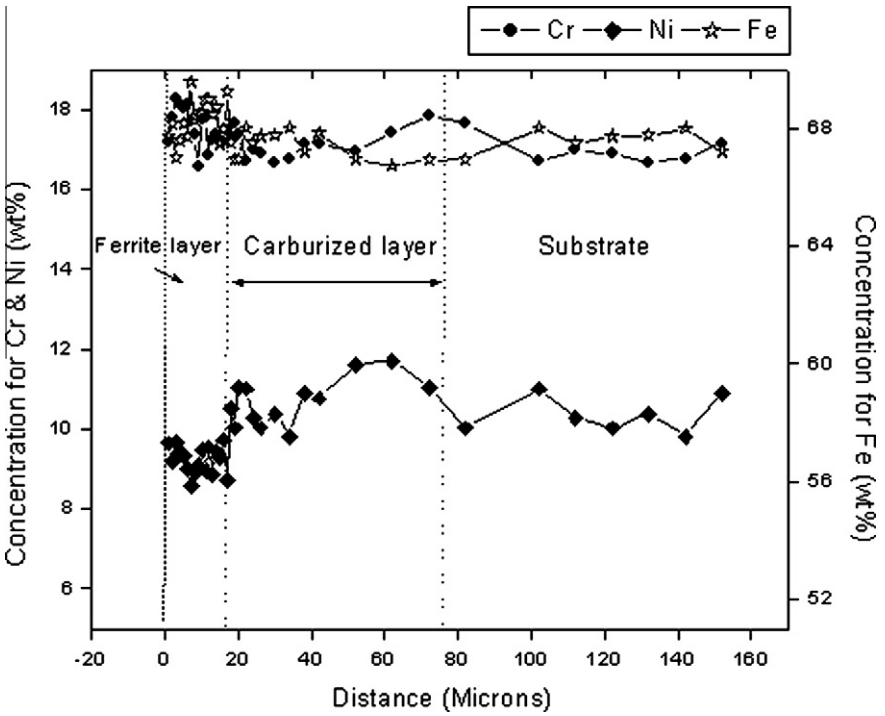

Fig. 7. Elemental concentration profiles for Cr, Fe and Ni showing Ni depletion on the surface.

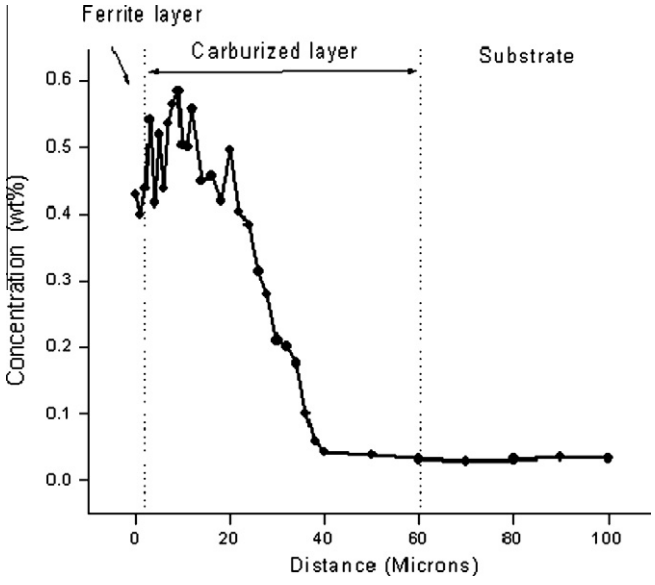

Fig. 8. Experimental carbon concentration profile showing a carburized layer up to a depth of ~60 μm from the surface.

than the a_C value reported (~0.001) [23] in Fe–18Cr–8Ni austenitic stainless steel containing 0.04% carbon. Hence in Indian sodium containing 25 wppm of carbon out of which 2 wppm is in solution, a_C will be much higher than 316LN austenitic stainless steel containing 0.03% of carbon leading to carburization at 798 K. Such a large difference in a_C is because of the strong dependence of a_C^{Na} (carbon activity in sodium) on temperature and C_{Na}^{sat}.

Carbon which diffuses to steel due to the activity gradient reacts with chromium to form a carburized zone having high volume fraction of $M_{23}C_6$ type of carbides. X-ray diffraction analysis (Fig. 5) has confirmed the presence of Cr rich $Cr_{23}C_6$ type of precipitates on the surface. $M_{23}C_6$ is the most stable carbide phase in austenitic stainless steel in the temperature range of 773–1073 K [24,25]. In the high temperature, high velocity section of the sodium loop only $M_{23}C_6$ precipitates have been detected in the structural material [26]. From the carbon concentration profile (Fig. 8) the carbon content in the carburized zone ($\gamma + M_{23}C_6$) is found to be ~0.5 wt%. The continuous decrease in carbon concentration within the carburized zone is due to the change in the stoichiometry of the carbide as understood from a study on carburization in multi element alloy systems [11]. In this work it is stated that since $Cr_{23}C_6$ has large solubility for Fe the Cr/Fe ratio will change continuously with the penetration depth. This change depends on the carbon concentration at a particular depth and free energy of formation of carbides with specific stoichiometry.

3.2. Analysis of the carburized layer – modeling studies

To simulate carburization profiles in an austenitic stainless steel (Fe–Cr–Ni–C system) a theoretical model developed by the authors [27] was used which was based on the finite difference method. The model has been further extended in this study to account for the simultaneous precipitation of Cr rich $M_{23}C_6$ type of carbides in addition to the diffusion of carbon in the matrix.

Even though carbon in sodium can exist in the form of atomic carbon, carbides, carbonitrides or cyanides [28], contribution from atomic carbon alone was considered since it is the most important species in sodium [29]. Initially calculations were performed to determine the change in total carbon concentration in the matrix using a model based on Fick's second law of diffusion [27]. The diffusion equations were later transformed to finite difference equations using one dimensional mesh points separated by space increment 'Δx' and time increment 'Δt'. One-dimensional finite difference mesh was assumed to consist of 200 mesh points. To minimize the error, width of the each mesh point Δx was kept as 0.001 mm. Time increment was calculated from the criteria

$$\Delta t \leqslant \frac{\Delta x^2}{2D} \tag{2}$$

Following boundary conditions were assumed in the calculation:

$C_1(x) = C_S$ at $x = 0$ (where C_S is the surface carbon concentration)
$C_1(x) = C_1(x-1)$ at $x = 201$

Values for the interaction parameter of carbon with a substitutional alloying element 'ε_C^M' were takes as follows: $\varepsilon_C^C = +1.09$, $\varepsilon_C^{Cr} = -19.64$ and $\varepsilon_C^{Ni} = 7.8$ [30]. Electron microprobe data (Figs. 7 and 8) was used for the concentration of alloying elements on the surface as well in the base material. In addition to the interaction parameters and elemental concentrations, values for diffusion coefficients are also required to proceed with the computation. In the earlier studies on modeling of carburization profiles [10,14] effective diffusion coefficient values were obtained after adjusting the experimental and computed profiles for a good fit. In this work the concentration dependant diffusivity values $D(c)$ were evaluated from the carbon concentration profile (Fig. 8) as follows:

- Based on the concentration of the base metal 'C_0' at infinity and 'C'-the concentration at a particular distance from the interface, a parameter 'u' was determined from the following equation:

$$\frac{C}{C_0} = erfc\ (u) \tag{3}$$

A concentration ratio curve was constructed between $\frac{x}{\sqrt{t}}$ ('x' is the diffusing distance) and 'u', from which the slope 'h' and intercept 'k' were determined. These values were substituted in the Hall's equation [31] to determine $D(c)$ value in the base material:

$$D(c) = \frac{1}{4h^2} + \frac{k\pi^{\frac{1}{2}}}{2h^2}\exp(u^2)erfcu \tag{4}$$

- In the carburized layer Den Broeder's method [32] was used to find $D(c)$ based on the following equation:

$$D(c) = \frac{1}{2t}\left(\frac{dx}{dc}\right)_{c'}\left\{(1-\psi)\int_{-\infty}^{x}(C(x)-C^-)dx + \psi\int_{x}^{+\infty}(C^+ - C(x))dx\right\} \tag{5}$$

where $\left(\frac{dx}{dc}\right)_{C'}$ indicates the inverse of the concentration gradient at a particular concentration C', $C(x)$ is the concentration at a particular distance 'x', C^- and C^+ are the concentrations on either side of the interface at infinity and $\psi = \frac{C(x)-C^-}{C^+-C^-}$ is the relative concentration.

Typical effective diffusion coefficient values used in the computation are given in Table. 2. Value of $D(c)$ for the base material (2.57×10^{-12} m^2/s) obtained using Halls' method agrees well with the effective diffusion coefficient value for AISI 316 stainless steel (2.2×10^{-12} m^2/s) reported in literature [10].

After obtaining the effective diffusion coefficient and interaction parameter values, total carbon concentration $C(x,t)$ at a particular mesh point 'x' and time 't' was calculated by using the following governing equations given in [27].

$$C_1[x,(t+\Delta t)] = C_1[x,t] + A + B \tag{6}$$

where

Table 2
Typical $D(c)$ values in the computation.

Region	$D(c)$ (m^2/s)
Carburized zone	2×10^{-11}
Near the interface	3.87×10^{-11}
Base material	2.57×10^{-12}

$$A = \frac{D_{11}\Delta t}{\Delta x^2}\{C_1[(x+1),t] - 2C_1[x,t] + C_1[(x-1),t]\}$$

and

$$B = \frac{D_{12}\Delta t}{\Delta x^2}\{C_2[(x+1),t] - 2C_2[x,t] + C_2[(x-1),t]\}$$

In the above equations C_1 and C_2 are the concentration for carbon and chromium in solution, D_{11} and D_{12} are the self diffusion coefficient and cross diffusion coefficient for carbon which are related by the following expression:

$$\frac{D_{12}}{D_{11}} \cong \varepsilon_{12}X_1 \tag{7}$$

where 'X' denotes the mole fraction for carbon. To account for the precipitation, only one type of carbide ($M_{23}C_6$) was considered. The solubility parameter given by Bongartz et al. [10] for a particular stoichiometry of $M_{23}C_6$ ($Cr_{16}Fe_7C_6$) has been used in the calculation. At a mesh point, amount of diffusing carbon was determined using the finite difference equation. From the solubility product carbon soluble in the matrix was determined. If this value was less than the amount of diffusing carbon, the difference in the carbon concentration was assumed to be tied in the carbide. Remaining carbon available in solution diffuses to the next mesh point. In this way total carbon concentration (carbon in the matrix + precipitates) was determined. A computer programme was written to solve the equations, the flowchart for which is given as Fig. 9. The computed carbon concentration profile was found to show reasonably good agreement with the experimental profile (Fig. 10).

Carbon diffusion profiles were simulated for different durations of exposure at a fixed temperature of 798 K. Fig. 11a clearly shows the increase in the thickness of the carburized layer with the time of exposure. From the carbon diffusion profiles thickness of the carburized layer was calculated and plotted as a function of time in Fig. 11b. Width of the carburized layer was found to

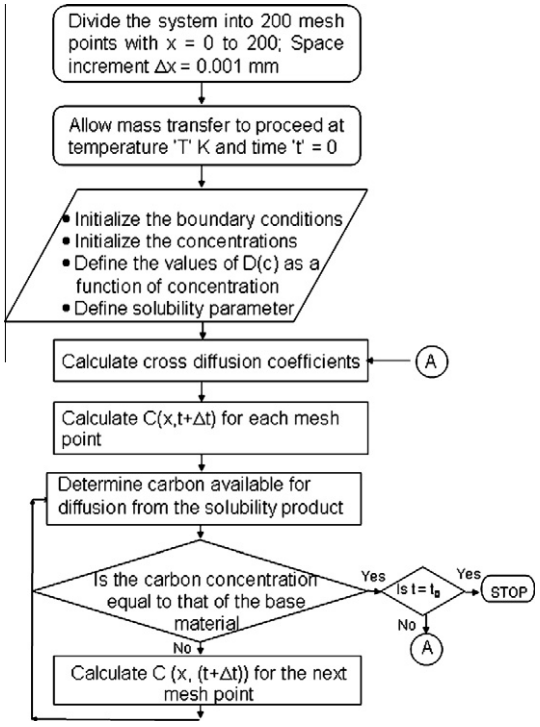

Fig. 9. Flowchart showing the steps involved in the computation of carbon diffusion profiles using finite difference method.

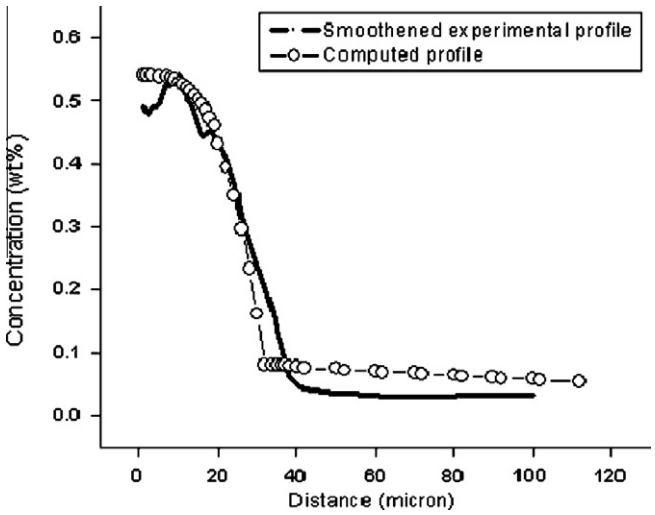

Fig. 10. Computed carbon diffusion profile showing a reasonable agreement with the superimposed smoothened experimental profile.

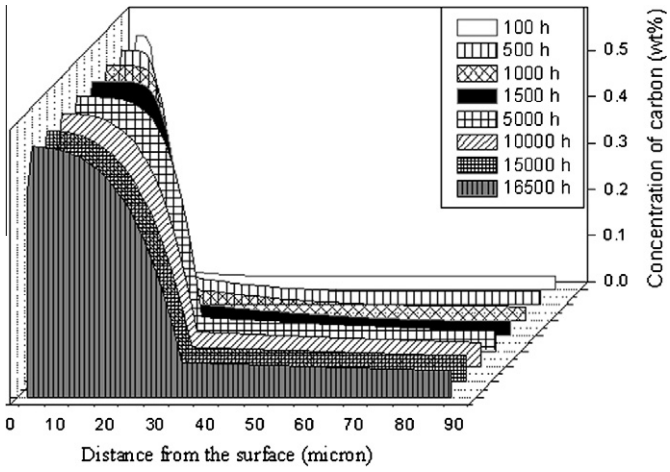

Fig. 11a. Computed carbon concentration profiles at a temperature of 798 K for different durations of exposure.

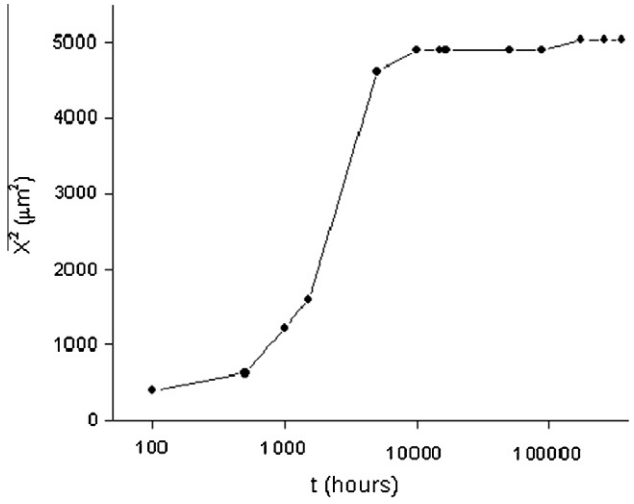

Fig. 11b. Plot of square of the thickness '*X*' of the carburized layer as a function of time '*t*' of exposure at 798 K.

increase with the exposure time till 10,000 h beyond which the change in the width slows down considerably. The model was also used to predict the carbon concentration profiles across the austenitic stainless steel after a period of 40 years. It was assumed that the carbon concentration had reached a dynamic equilibrium value of 0.5 wt% at the surface and remained constant by further exposure to sodium. Such an assumption is valid since the total carbon concentration in sodium is in large excess and conversion of undissolved carbon to dissolved carbon facilitates the maintenance of constant carbon activity. Since diffusion of carbon on the surface has to take place in a matrix consisting of high number density of carbides, its diffusion is considerably slowed down ($D(c)$ of the order of 10^{-15} m^2/s) and thickness of the carburized layer after a period of 40 years was found to be only 160 μm.

Even though finite difference method satisfactorily predicted the carbon concentration profiles it has several disadvantages arising out of the assumptions made during calculation as follows: (1) Dynamic equilibrium value for carbon assumed in the calculation was much less than the value suggested in literature [24] for a Fe–18Cr–8Ni austenitic stainless steel for a temperature of 873 K (2) Even though precipitation of carbides was considered along with diffusion, solubility data was obtained for a specific stoichiometry of $M_{23}C_6$ carbide in a different alloy system (Fe–32Ni–8Cr). This may lead to overestimation or under estimation of zone width if the stoichiometry of carbide changes and (3) change in the concentration of substitutional alloying element like Cr due to precipitation and the consequent change in the stoichiometry of the carbide was not considered.

To deal with diffusion in multiphase systems more accurately, numerical techniques incorporating Dictra and Thermo-calc softwares have been developed [12,33]. In this model the carbides were considered as dispersed particles in a continuous matrix where the diffusion of one or more species occurs. Equilibrium was always assumed to be maintained between the dispersed phases and the matrix. In the simulation for each time increment Δt, calculation was performed in two steps (1) the diffusion step which was identical to the solution of Fick's second law of diffusion in a single phase precipitate free matrix and (2) the equilibrium step based on Gibbs energy minimization where the precipitates were assumed as source or sink for the solutes. Equilibrium calculations were used to determine the fraction and composition of $M_{23}C_6$ precipitates present in the matrix.

In the present work MOB2 version of the kinetic database was used to get the values for mobility, diffusion coefficient and activation energy. For the thermodynamic data, information from the following ternary and quaternary systems were used: Fe–Cr–C and Ni–Cr–C [34], Cr–Fe–Ni [35], C–Fe–Ni [36] and Fe–Cr–Ni–C [37]. The phases were described using regular solution model with several components and sublattices as follows: (1) γ phase as fcc phase with two sublattices namely $(Fe–Cr–Ni)_1$ and $(C, Va)_1$ where Va denotes vacancies and (2) $M_{23}C_6$ as a stoichiometric phase with three sublattices namely $(Cr, Fe)_{20}$, $(Cr, Fe, Mo)_3$ and C_6. The simulation was performed for an exposure temperature of 798 K and time of 16,000 h. Diffusion calculations were performed in one dimensional mesh with the maximum space and time increments takes as $\Delta x = 1$ μm and $\Delta t = 5$ s respectively.

Fig. 12a shows a comparison of the carbon concentration profiles obtained using electron microprobe, FDM and Dictra. It is clear from the figure that FDM based simulation matches well with the experimentally obtained profile. This is not surprising since the computation had several input parameters from experiments like surface carbon content, $D(c)$ and base material composition. Computations based on Dictra were found to predict only the carburized zone width accurately. Since the formation of a ferrite zone

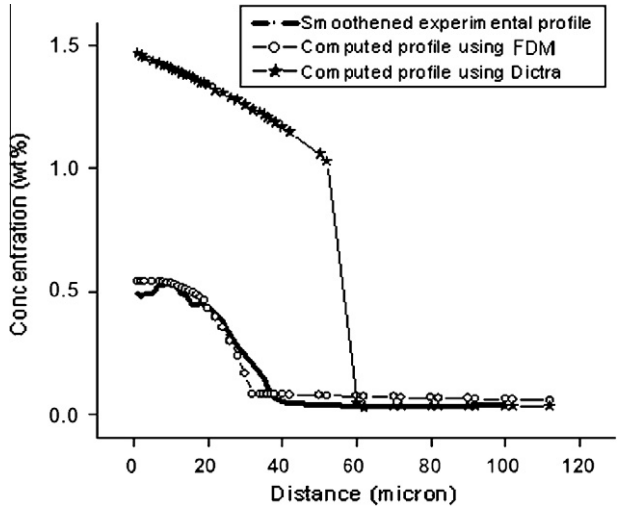

Fig. 12a. Comparison of the carbon concentration profiles obtained using electron microprobe, FDM and Dictra at a temperature of 798 K for 16,000 h.

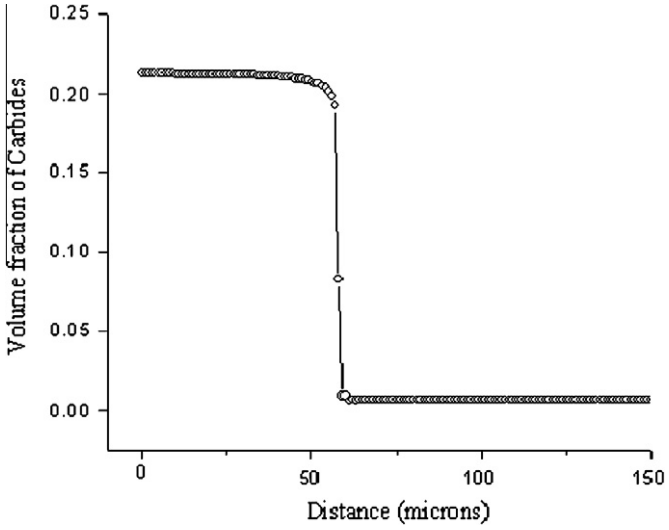

Fig. 12b. Volume fraction of $M_{23}C_6$ carbides computed using a numerical technique based on Dictra and Thermocalc at a temperature of 798 K for 16,000 h.

due to the leaching of substitutional alloying elements was not considered the surface carbon concentration was getting overestimated. Dictra based simulation can be made more accurate by adopting a cell model for incorporating the diffusion of carbon in bcc and fcc systems which will be attempted in future. Fig. 12b shows the volume fraction of $M_{23}C_6$ precipitates plotted as a function of distance from the surface of austenitic stainless steel exposed to sodium. Equilibrium carbon concentration on the surface (~1.4 wt%) agreed with the data reported in literature for austenitic steels equilibrated in sodium at the same temperature [24]. Volume fraction of the carbides remained constant throughout the carburized zone whereas a continuous decrease in carbon concentration indicated a possible change in the stoichiometry of the carbides.

Prediction of carburization or decarburization of an austenitic stainless steel when exposed to sodium is significant since changes in mechanical properties due to carbon diffusion have been reported by many [21,38–40]. Although the model presented here is with respect to carburization of austenitic stainless steel when exposed to sodium, it can be applied to any diffusion process where the diffusing species undergoes chemical reaction with another constituent element. Even though width of the carburized zone has been predicted using the model, two other phenomena namely leaching and formation of degraded layer which affect the wall thickness of the exposed material has not been considered. For oxygen content in sodium in the range of 2–9 wppm the recommended expression for loss of the material due to leaching is [13]

$$S(\mu m/year) = 25\ \exp\ (5.62 + 3.45\log_{10}[O] - 75312/RT) \quad (8)$$

where $[O]$ is the concentration of oxygen in sodium in wppm, R is the gas constant in $JK^{-1}\ mol^{-1}$ and T is the temperature in K. From the above expression loss of material due to leaching at a temperature of 798 K was found to be 4.6 μm for 16,000 h. Similarly the thickness of the ferrite layer ('Y') in 316LN stainless steel at 798 K for 16,000 h was calculated as 11.4 μm using the following expression given in literature [13].

$$Y(\mu m) = -97.1 + 25.8\log_{10}(t) \quad (9)$$

where 't' is the time of exposure in hours. This value matches closely with the experimentally observed thickness of the ferrite layer (Fig. 4) after 16,000 h of sodium exposure. Combining the above information with the predicted thickness of the carburized layer total affected thickness of 316LN austenitic stainless steel due to sodium exposure for 16,000 h was estimated as ~76 μm. For 40 years the total thickness of the component which will be affected due to leaching, formation of the degraded layer and carburized layer was estimated as ~310 μm.

The above described results were compared with those obtained in a monometallic loop [13]. Type 316LN stainless steel samples were exposed to flowing sodium in monometallic loop after exposures of type 316 stainless steel for 16,000 h, while exposures of type 316LN stainless steel in bi-metallic loop was in freshly filled sodium. Considerable difference was observed in the carburization behavior of 316LN stainless steel in BIM loop and MTL. The steel was getting carburized to a greater depth (~100 μm) in the BIM loop compare to MTL (~40 μm). Higher carburization in bi-metallic loop cannot be assigned to the presence of modified 9Cr–1Mo steel since the latter also got carburized. However the reason could be due to possible changes in sodium chemistry vis-à-vis carbon content.

4. Conclusion

1. Microstructural and microchemical modification on the surface of sodium exposed 316LN austenitic stainless steel was studied.
2. A modified layer of ~10 μm width having ferrite structure was detected on the surface of sodium exposed steel. Below the modified surface layer presence of carburized layer to a distance of ~60 μm was confirmed from electron microprobe based investigations.
3. Carburization profiles were predicted using a model based on finite difference method which showed a reasonably good match with the experimental profile. Calculations predicted ~310 μm as the total loss in the thickness of the material due to leaching, formation of ferrite and carburized layer when exposed to sodium at 798 K for 40 years.
4. Equilibrium calculations based on Dictra and Thermo-calc softwares which incorporate the kinetic as well as the thermodynamic information of the system were used for predicting the carburization profiles. In addition to the width of the carburized zone, change in the volume fraction of the carbides as a function of distance also was determined.

Acknowledgements

The authors thank Dr. Baldev Raj, Director IGCAR and Dr. T. Jayakumar, Group Director MMG for their support throughout the period of this project. The authors would like to thank Dr. K. Madan Gopal of BARC, Smt. S. Kalavathi and Shri. R.V. Subba Rao of IGCAR for their support during the course of this Project.

References

[1] S. Rajendran Pillai, H.S. Khatak, Corrosion of Austenitic Stainless Steels: Mechanisms, Mitigation and Monitoring, Narosa Publishing, New Delhi, 2002.
[2] N. Sivai Bharasi, K. Thyagarajan, H. Shaikh, A.K. Balamurugan, Santanu Bera, S. Kalavathy, K. Gurumurthy, A.K. Tyagi, R.K. Dayal, K.K. Rajan, H.S. Khatak, J. Nucl. Mater. 377 (2008) 378.
[3] T. Gnanasekaran, C.K. Mathews, J. Nucl. Mater. 140 (3) (1986) 202.
[4] K. Natesan, Meimei Li, O.K. Chopra, S. Majumdar, J. Nucl. Mater. 392 (2009) 243.
[5] T. Suzuki, I. Mutoh, T. Yagi, Y. Ikenaga, J. Nucl. Mater. 139 (2) (1986) 97.
[6] H. Huthman, G. Menken, H.U. Borgstedt, T. Tass, in: Proceedings, Second International Conference on Liquid Metal Technology in Energy Production, vol. 2, Richland, Washington, 1980.
[7] Tadayuki Kataoka, Keishi Matsumoto, J. Nucl. Sci. Technol. 16 (6) (1979) 416.
[8] K. Natesan, T.F. Kassner, Nucl. Technol. 19 (1973) 46.
[9] D. Farkas, J. Delgado, Scripta Metall. 17 (1983) 261.
[10] K. Bongartz, D.F. Lupton, H. Schuster, Metall. Trans. 11A (1980) 1883.
[11] K. Bongartz, W.J. Quadakkers, R. Schulten, H. Nickel, Metall. Trans. 20A (1989) 1021.
[12] A. Engstrom, L. Hoglund, J. Agren, Metall. Mater. Trans. 25A (1994) 1127.
[13] N. Sivaibharasi, K. Thyagarajan, H. Shaikh, A.K. Balamurugan, S. Bera, S. Kalavathy, K. Gurumurthy, A.K. Tyagi, R.K. Dayal, K.K. Rajan, H.S. Khatak, J. Nucl. Mater. 377 (2008) 378.
[14] S. Rajendran Pillai, H.S. Khatak, N. Sivai Barasi, A.K. Tyagi, J.B. Gnanamoorthy, R.D. Kale, K. Swaminathan, M. Rajan, K.K. Rajan, Trans. Indian Inst. Metals 50 (1) (1997) 103.
[15] C. Sudha, R. Anand, S. Saroja, M. Vijayalakshmi. Trans. Indian Inst. Metals, in press.
[16] S. Rajendran Pillai, H.S. Khatak, J.B. Gnanamoorthy, S. Velmurugan, A.K. Tyagi, R.D. Kale, K. Swaminathan, M. Rajan, K.K. Rajan, Mater. Sci. Technol. 13 (11) (1997) 945.
[17] J.F. Moulder, W.F. Stickle, P.E. Sobol, K.D. Bomben, Handbook of X-ray Photoelectron Spectroscopy, Physical Electronics Inc., USA, 1995.
[18] M. Detroye, F. Reniers, C. Buess Herman, J. Vereecken, Appl. Surf. Sci. 144–145 (1999) 78.
[19] C.O.A. Olsson, D. Landolt, Electrochim. Acta 48 (2003) 1093.
[20] T.D. Claar, Reactor Technol. 13 (1970) 124.
[21] A.M. Azad, O.M. Sreedharan, J.B. Gnanamoorthy, J. Nucl. Mater. 151 (3) (1988) 301.
[22] R.B. Snyder, K. Natesan, T.F. Kassner, J. Nucl. Mater. 50 (1974) 259.
[23] C.K. Mathews, T. Gnanasekaran, S. Rajendran Pillai, Trans. Indian Inst. Metals 40 (1) (1987) 89.
[24] K. Natesan, T.F. Kassner, J. Nucl. Mater. 37 (1970) 223.
[25] <http://www.msm.cam.ac.uk/phase-trans/2005/Stainless_steels/stainless.html.>
[26] A.W. Thorley, A. Blundell, J.A. Bardsley, Material Behavior and Physical Chemistry in Liquid Metal Systems, Plenum Press, Newyork, 1981.
[27] R. Anand, C. Sudha, T. Karthikeyan, A.L.E. Terrance, S. Saroja, M. Vijayalakshmi, J. Mater. Sci. 44 (1) (2009) 257.
[28] H.S. Khatak, in: Proceedings, International Conference on Emerging Trends in Corrosion Control, vol. 1, New Delhi, India, 1999.
[29] F.B. Litton, A.E. Morris, J. Less Common Metals 22 (1970) 71.
[30] J. Kucera, K. Stransky, J. Dojiva, Mater. Sci. Eng. A125 (1990) 75.
[31] Lewis D. Hall, J. Chem. Phys. 21 (1) (1953) 87.
[32] F.J.A. Den Broeder, Scripta Metall. 3 (1969) 321.
[33] J.O. Andersson, T. Helander, L. Höglund, P. Shi, B. Sundman, Calphad 26 (2002) 273.
[34] Byeong-Joo Lee, Calphad 16 (2) (1992) 121.
[35] J. Miettinen, Calphad 23 (2) (1999) 231.
[36] A. Gabriel, P. Gustafson, I. Ansara, Calphad 11 (2) (1987) 203.
[37] M. Hillert, C. Qiu, Metall. Trans. A 3 (5) (1992) 1593.
[38] A.V. Karpov, Kh. Kononyuk, L.I. Mamaev, Yu.L. Kulikov, At. Energy 91 (5) (2001) 951.
[39] S. Rajendran Pillai, H.S. Khatak, N. Sivaibarasi, A.L.E. Terrance, R.D. Kale, M. Rajan, K.K. Rajan, in: Proceedings, International Symposium on Materials Ageing and Life Management, Allied Publishers Ltd., Chennai, India, 2000.
[40] N. Sivaibarasi, K. Thyagarajan, H. Shaikh, R.K. Dayal, Behaviour of Structural Materials in a Bi-metallic Sodium Loop at 798 K, Internal Report, Indira Gandhi Centre for Atomic Research, Corrosion Science and Technology Division, Kalpakkam, 2008.